ARTICLE

Identification of distinctive structural and optoelectronic properties of Bi_2O_3 polymorphs controlled by tantalum addition

Received 00th January 20xx,
Accepted 00th January 20xx

DOI: 10.1039/x0xx00000x

Taro Saito,[a]† Rafia Ahmad,[b]† Fuminao Kishimoto,[a] Tomohiro Higashi,[c] Masao Katayama,[d] Luigi Cavallo,*[b] Kazuhiro Takanabe*[a]

Diverse crystal phases of bismuth (Bi) oxides induced by the addition of different amounts of tantalum (Ta) were synthesized. Optoelectronic and redox properties were quantitatively investigated using combined experimental and computational approaches. Synthesis conditions that transform α-Bi_2O_3 to β-Bi_2O_3 and δ-Bi_2O_3 in terms of Ta quantity, as well as synthesis temperatures, are identified and demonstrated. Phase transition behavior and crystal structures were characterized with *in situ* high temperature X-ray diffraction (XRD) and thermogravimetry–differential thermal analysis (TG/DTA), X-ray absorption near edge structures (XANES), and extended X-ray absorption fine structures (EXAFS). Density functional theory calculations employing HSE exchange-correlation functional with spin-orbit coupling quantitively simulated the optoelectronic properties and band structures of the β-Bi_2O_3 and δ-Bi_2O_3. Along with the absorption coefficient and density of states, effective masses and dielectric constants were elucidated. The characterization confirmed the distortion of Ta–O bonds in the Ta-supplemented β-Bi_2O_3 and the substitutional positions of the Bi and Ta atoms in the δ-Bi_2O_3 and Bi_3TaO_7 compounds. Reducibility of these oxides was strongly influenced by the crystal phase confirmed by temperature-programmed reduction (TPR) analysis. These findings should be usable as a bismuth oxides' benchmark for optoelectronic applications as well as thermal catalysis as the redox active center or the support.

Introduction

Bi_2O_3 is one of the polymorphous oxides, which exhibits broad applications such as solid-state electrocatalysis,[1–6] pigment,[7], and photocatalytic reaction.[8–27] To date, four different crystal phases have been reported: α phase (monoclinic), β phase (tetragonal), γ phase (cubic), and δ phase (cubic). Among the polymorphs, the α phase is the most stable phase at room temperature. The high-temperature–stable δ phase is transformed to the β or γ phase while cooling, which results in the further transformation to the α phase at room temperature.[28] While the δ phase shows a high O^{2-} ion conductivity, applicable to mid-temperature electrocatalysis at 300–500 °C,[1–5] β-Bi_2O_3 attracts attention as a photocatalyst due to a narrow bandgap of ~2.2 eV.[8–12]

Solid-state synthesis of pure Bi_2O_3 has been well executed in the literature.[28] Knowing the melting point of Bi_2O_3 to be ~830 °C, phase transition temperatures have been studied in detail. Nevertheless, selective synthesis of specific phases from pure Bi_2O_3 remains challenging. By doping α-Bi_2O_3 with a trace amount of oxides, such as Ta_2O_5, CeO_2, ZrO_2, EuO_x, TiO_x, and MnO_x[5,7,29–33], a solid-state reaction at a high temperature becomes possible to make metastable β-, γ-, and δ-phases recoverable for successive applications. Recently, Masui and coworkers reported having mixed Ta_2O_5 into α-Bi_2O_3 to synthesize the β- and δ-phase, and its unique bandgap narrowing has been recognized for pigment application.[7] This bandgap with a visible light response may be suitable for solar energy conversion, but the investigation of β-Bi_2O_3 as a photocatalyst, especially application for photosynthetic reaction, has been limited.[9] The details of how the Ta induces the crystal phase transition and narrows the bandgap also remain unclarified.

The purpose of this study is to provide not only explicit synthesis protocols for each crystal structure, but also quantitative analysis on various optoelectronic and redox properties of the bismuth oxides. Different Bi_2O_3 phases and Bi_3TaO_7 were successfully attained by varying the Ta/Bi ratio (0.020–0.333). The obtained materials were characterized by in situ X-ray diffraction (XRD), X-ray absorption spectroscopy (XAS), diffuse-reflectance ultraviolet-visible spectroscopy (DR-UV-vis), and photoelectron spectroscopy in air (PESA). The optoelectronic structure was studied both experimentally and theoretically to understand their density of state (DOS), dielectric properties, and effective masses.

[a] *Department of Chemical System Engineering, School of Engineering, The University of Tokyo, 7-3-1, Hongo, Bunkyo-ku, Tokyo 113-8656, Japan.*
[b] *King Abdullah University of Science and Technology (KAUST), KAUST Catalysis Center (KCC), 4700 KAUST, Thuwal 23955-6900, Saudi Arabia.*
[c] *Institute for Tenure Track Promotion, University of Miyazaki, Nishi 1-1 Gakuen-Kibanadai, Miyazaki 889-2192, Japan.*
[d] *Environmental Science Center, Department of Chemical System Engineering, The University of Tokyo, 7-3-1, Hongo, Bunkyo-ku, Tokyo 113-8656, Japan.*
† These authors contributed equally.
Electronic Supplementary Information (ESI) available: [details of any supplementary information available should be included here]. See DOI: 10.1039/x0xx00000x

Photoelectrochemical (PEC) measurements and temperature-programmed reduction (TPR) analyses were conducted.

Experimental and theoretical

Synthesis

Ta_2O_5 (99.9%, Kojundo Chemical Laboratory Co., Ltd.) was mixed with Bi_2O_3 (98.0+%, FUJIFILM Wako Pure Chemical Corporation) ($0.020 \leq Ta/Bi \leq 0.333$) using a mortar and pestle. Heat treatment was usually conducted at 850 °C, with a heating rate of 10 °C min^{-1} and was held at this temperature for 5 h in a muffle furnace in the air. During the heat treatments, the mixtures were placed on an Alumina boat (Nikkato, SSA-S grade, Al_2O_3 99.6%) to prevent contamination of silica components. Then, the samples were cooled naturally in the furnace by turning off the electric power. The samples were ground in an Alumina boat prior to characterizations.

X-ray Diffraction

The powder XRD patterns were collected using Rigaku Ultima III equipped with a copper (Cu) X-ray source operated at 40 kV and 40 mA. The diffractometer was configured with a 1/2° divergence slit limited to 10 mm, an open scattering slit, an open receiving slit, and a nickel (Ni) filter to attenuate contributions from Cu-K_β fluorescence. The data sets were acquired in continuous scanning mode (20° min^{-1}) with the integration step size of 0.02°; however, when focusing on certain peaks (i.e., only around 2θ = 26–29°), these parameters were set to 1° min^{-1} and 0.01°, respectively. The peak positions were calibrated using the secondary peak of silicon (Si) (standard, 220, 47.2660°, cubic, Fd-3m). In situ high-temperature XRD was performed using an attachment (Reactor-X, Rigaku) equipped with an infrared heater connected to its controller (PTC EVO, Rigaku) and an external power source (Thermo plus EVO PU-4K CE, Rigaku). An infrared reflector was attached to assist in heating the sample, while the attachments were continuously cooled with circulating water and both an external and internal fan. With this setup, the peak positions were calibrated using the secondary peak of Si powder (Wako, 220, 47.2660°, cubic, Fd-3m) at room temperature. The temperature was increased with a heating rate of 10 °C min^{-1} from the room temperature to 830 °C and 2 °C min^{-1} from 830 °C to 850 °C to prevent the cell from overheating. The temperature was decreased with a cooling rate of 10 °C min^{-1} to 25 °C, and the determined temperature was held for 5 min before each measurement. All measurements were conducted by flowing a mixture of 80 mL min^{-1} argon (Ar) and 20 mL min^{-1} O_2. The temperature was corrected by using the α to δ phase transition peak (in the heating process) of Bi_2O_3 (98.0+%, Wako Pure Chemical Corporation) at 735 °C.

X-ray Absorption Spectroscopy

Bi L_3-edge and Ta L_3-edge XAS were recorded at the bending magnet XAFS beamline, BL01B1 at SPring-8 (Hyogo, Japan). Experiments were performed at room temperature and in the transmission mode using the ionization chambers. Bi_2O_3 and Ta_2O_5 were used as references. The powder samples were thoroughly ground with boron nitride in an agate mortar, and 10-mm–diameter pellets were made. The amount of the boron nitride was ~90 mg to ensure the pellets could be handled without breaking. The EXAFS spectra were analyzed using the HORAE-IFEFFIT (Athena) program package. This program enabled us to normalize the absorption coefficient, $\mu(k)$, and to separate the oscillatory EXAFS, $\chi(k)$, from the absorption background. Before the normalization, the pre-edge range of the spectra for Bi and Ta L_3 edges were flattened using the energy range of −210 to −60 keV and −200 to −60 keV, respectively. The data sets for Bi and Ta L_3 edges were normalized using the energy range of 50–880 keV (4.0–71.0 $Å^{-1}$) and 200–1000 eV (16.1–80.7 $Å^{-1}$), respectively. Then, the background was calculated from the data in energy ranges of 0–15 $Å^{-1}$ (0–857 eV) for Bi L_3 edges and 0–17 $Å^{-1}$ (0–1001 eV) for Ta L_3 edges. All data were Fourier-transformed using the same k range, k = 3–12 $Å^{-1}$, k weighting of 2 and a hanning k window and plotted with k weighting of 3. The theoretical radial distribution functions were calculated using the Visual Molecular Dynamics (VMD) program (version 1.9.4a49).[34]

Band Position Determination

DR-UV-vis and PESA were performed to determine the band alignment of the conduction band minimum (CBM) and the valence band maximum (VBM) positions of the synthesized samples. DR-UV-vis spectroscopy was performed on a JASCO model V-770 spectrophotometer equipped with an integrating sphere. The reflectance spectra were scanned over the range of 200–1000 nm with a scan speed of 400 nm min^{-1} and a bandwidth of 2.0 nm for the ultraviolet/visible region and 8.0 nm for the near-infrared region. The reflectance spectra were referred to the background reflectance of $BaSO_4$ powder. The contributions of scattering were removed by the Kubelka-Munk function, $F(R_\infty)$. Followed by the calculation of the bandgap energy, the absorption edge was determined by the intercept of the straight line extrapolated to the $F(R_\infty)$ vs wavelength.

The valence band positions were determined by PESA (AC-3 photoelectron spectrometer, Riken Keiki Co., Ltd.). The obtained spectra were calibrated based on the work function of gold (Au) (5.30 eV vs. vacuum).[35] The yield of the photoelectrons was measured for 30 s at every 0.1 eV step in the range of 4.0–7.0 eV of irradiation UV light. The valence band potentials, obtained as the potentials relative to the absolute vacuum potential, were converted to the standard hydrogen potentials ($E_{SHE} = E_{abs} - 4.44$ V). The conduction band positions were calculated from the valence band positions, and the bandgaps were determined by PESA and DR-UV-vis spectroscopy.

Photoluminescence

Photoluminescence (PL) spectroscopy was performed on a JASCO model FP-8500 fluorescence spectrometer operated at liquid nitrogen temperature under the ambient pressure. The excitation and emission had a 5-nm bandwidth. The spectra were scanned at the speed of 1000 nm min^{-1} with medium level

sensitivity and 50 ms of response at every 0.1-nm interval and accumulated over 10 cycles.

Thermogravimetry/Differential Thermal Analysis

TG/DTA was performed to investigate the phase transition processes of Ta_2O_5-supplemented Bi_2O_3 *in situ*. TG/DTA using Thermo plus EVO2 series TG-DTA 8120 (Rigaku) in the atmosphere of the residual air in the chamber without flow. All measurements were performed with 10 °C min^{-1} heating and cooling rates up to 850 °C. As the sample (8–10 mg of the Bi_2O_3 powder or the mixture of Bi_2O_3 and Ta_2O_5 powders mixed at the stoichiometric amounts [Ta/Bi = 0.05, 0.10]) was placed in an open platinum pan. An open and empty platinum pan was used as the reference.

Scanning Electron Microscopy (SEM) and Elemental Analysis

The morphologies, particle sizes, and the layered structure of the particulate photoelectrodes were examined by high-resolution field emission SEM (FE-SEM; JEOL, JSM-IT800) equipped with a secondary electron detector. Energy-dispersive X-ray spectroscopy (EDS) was conducted with an EDS detector (Ultim Max, Oxford Instruments).

Computational Method

All calculations were performed using the Vienna Ab initio Simulation Package (VASP),[36,37] with the projector augment wave (PAW) method.[38] Calculations were performed with cut-off energy set to 400 eV. Brillouin zone sampling was performed using Monkhorst and Pack scheme.[39] We completely relaxed the bulk unit cell of β-Bi_2O_3 in its tetragonal structure with space group P-421*c*, which contains 8 Bi atoms and 12 oxygen (O) atoms. δ-Bi_2O_3 has the cubic fluorite structure with space group of Fm3m. The unit cell contains two Bi_2O_3 formulas. The valence atomic configurations are $5d^{10}\,6s^2\,6p^3$ for Bi and $2s^2\,2p^4$ for O atoms. Geometry optimizations were terminated when the energy and force on each ion were reduced below 10^{-6} eV and 0.02 eV/Å, and the optimized structures were then used to calculate the electronic structures. Hybrid DFT calculation was performed at a single point at the generalized gradient approximation (GGA) lattice geometry.[40] Firstly, the GGA scheme was employed for the fully-relaxed structural optimization. Then, the screened-exchange hybrid functional of Heyd, Scuseria, and Ernzerhof (HSE06),[41,42] representing the electronic exchange–correlation energy, was adopted during calculation of the electronic and optical properties. The spin–orbit coupling (SOC) effect was taken into consideration through the second variational method because of the relativistic effect in Bi atoms.[43] More details of the computational modeling of surfaces and of the methodology used to calculate the optical properties can be found in the Supporting Information.

Electrochemical (EC) and Photoelectrochemical (PEC) Measurements

To conduct EC and PEC measurements, particulate photoelectrodes were fabricated through previously reported particle transfer methods.[44] The multilayers of photocatalyst particles were deposited on a glass plate by drop-casting and drying its suspension in isopropanol several times, resulting in approximately 10 mg cm^{-2} in amount. Subsequently, 200 nm-thick–Ti and 3–4-μm–thick-Sn were sequentially deposited on the particles through an electron beam deposition (ULVAC) to prepare the assembly of photocatalysts with a Ti–Sn conductive layer. The obtained assembly of particles and the Ti–Sn layer adhering to them were peeled off from the glass plate, and the excess number of unused particles piled up on the particles were removed by ultrasonication in ethanol. The film electrode was fixed on another glass plate using carbon tape. Finally, the film was connected to a lead wire using indium solder, after which its unnecessary part was covered with epoxy resin for insulation. The geometrical electrode areas of the photoelectrodes were approximately 0.20–0.30 cm^2. EC and PEC measurements for the particulate-photoelectrodes were performed by the three-electrode configuration under argon (Ar) gas atmosphere at a temperature of 25 °C. Hg/Hg_2Cl_2/saturated KCl reference electrode (BAS Inc., RE-2BP, 241 mV vs. RHE at 25 °C) and coiled-Pt wire counter electrode were connected to a potentiostat (SP-150, BioLogic Science Instruments). Prior to the PEC measurements, a CoO_x catalyst promoting the carrier transfer at the solid–liquid interface was electrodeposited in the light on the surface of the particulate-photoelectrodes. A solar simulator (XES-40S2, SAN-EI Electric Co., Ltd.) equipped with an AM 1.5G filter was used as the light source, and the light intensity was adjusted to 100 mW cm^{-2} (1 sun). The electrolyte was made by saturating $Co(NO_3)_2{\cdot}6H_2O$ (0.1 M, 99.5%, Wako) in a 1 M potassium phosphate buffer solution. The pH of the buffer was adjusted to 7.0 by adding a potassium hydroxide (KOH; > 85%, Sigma-Aldrich) solution into a phosphoric acid (H_3PO_4, ≥ 85 wt. % in H_2O, Sigma-Aldrich) aqueous solution. The electrodeposition was performed at a constant current density of 50 μA cm^{-2} for 5 min in the simulated solar light (AM 1.5G). CoO_x deposited or not deposited particle-transferred working electrodes with an area of approximately 0.2–0.3 cm^2 were positioned in a glass cell. The electrolyte was a 1M potassium borate buffer (pH 9.0) aqueous solution. The pH was adjusted to 9.0 by adding a KOH (≥ 85%, Sigma-Aldrich) solution into a boric acid (H_3BO_3, ≥ 99.5 wt. % in H_2O, Sigma-Aldrich) aqueous solution. For LSV measurements, 0.1 M of Na_2SO_3 was added as a hole scavenger. PEC measurements employed a Xe-lamp (MAX-303 Xenon Light Source, 300 W, Asahi Spectra), with a UV-VIS miler module and a cut-off filter (HOYA L42) as the light source ($420 < \lambda < 650$ nm).

Temperature-Programmed Reduction

TPR equipment consisted of mass flow controllers (KOFLOC, model 3660) and a U-shaped quartz reactor inside an oven. Samples were treated in flowing Ar (20 mL min^{-1}) by increasing their temperature to 400 °C at 40 °C min^{-1} and holding for 1 h. After cooling to room temperature, the Ar stream was replaced with the reducing gas, 4% H_2 in Ar (20 mL min^{-1}). The

temperature was increased with a heating rate of 10 °C min^{-1} from the room temperature to 850 °C, and the H_2 concentration was monitored by a GC (GC-8A, TCD, Shimadzu) connected to the outlet of the reactor.

Results and discussion

Synthesis and Structural Characterizations of β- and δ-Bi_2O_3 and Bi_3TaO_7

The formation process of the β-Bi_2O_3:Ta (5%) and the δ-Bi_2O_3:Ta (10%) in the solid-state reaction was studied by DTA and *in situ* high temperature XRD measurements. Figure 1 shows the DTA curves of the pure Bi_2O_3, mixture of Bi_2O_3 and Ta_2O_5 at the ratio of Ta/Bi of 0.05 and 0.10, in this order. Figure 2 shows *in situ* high temperature XRD patterns for the samples at Ta/Bi = 0 (Figure 2a,b) and 0.050 (Figure 2c,d). Upon heating the samples, all of the samples show endothermic peaks at 735 °C (Figure 1). Accordingly, the new peak assignable to δ-Bi_2O_3 appeared (Figure 2a), clearly indicating the α to δ transition at this temperature. Pure Bi_2O_3 shows additional endothermic peak at 830 °C, which can be attributed to melting of δ-Bi_2O_3.[28] Lack of the melting behavior with Ta addition suggests that the melting point of Bi_2O_3 is higher than 850 °C. Subsequent decreases in temperature provided substantial differences in phase transition by varied Ta addition. For pure Bi_2O_3 (Ta/Bi = 0) in Figure 1, the DTA curve in the cooling process underwent two exothermic peaks of curding at 830 °C and at 620 °C. As a peak at 830 °C is likely solidification, consistent with the literature,[28] *in situ* XRD measurement clearly identified that a δ-to-α transition occurred (Figure 2b), indicating that the original state was recovered for the heating–cooling cycle. For the sample with Ta/Bi = 0.050, an exothermic peak at 580 °C (Figure 1) corresponded to the δ-to-β transition (Figure 2d), the phase that was not obtained without Ta addition. For the sample with Ta/Bi = 0.100, the DTA curve (Figure 1) did not show any pronounced peaks while cooling. This indicates that the δ phase of the Ta-supplemented Bi_2O_3 was maintained during the cooling process.

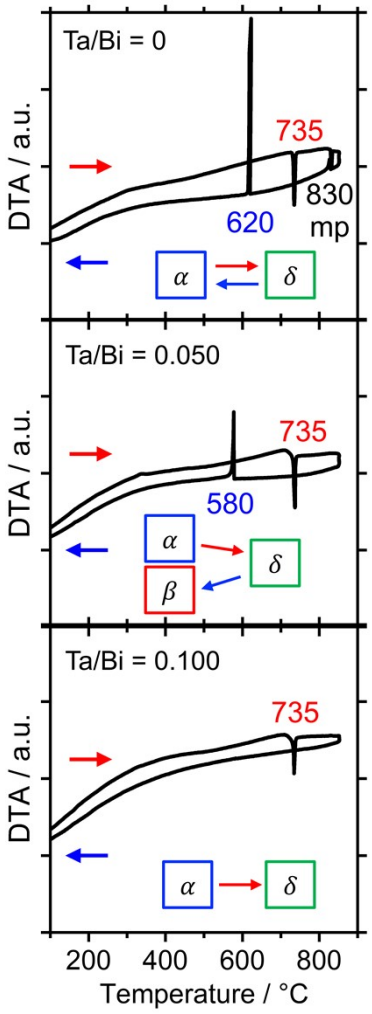

Figure 1. DTA curves of the Bi_2O_3 samples with Ta/Bi ratios of 0, 0.050, and 0.100, in this order. The temperature was increased and subsequently decreased at the rate of 10 °C min^{-1} in the flowing air.

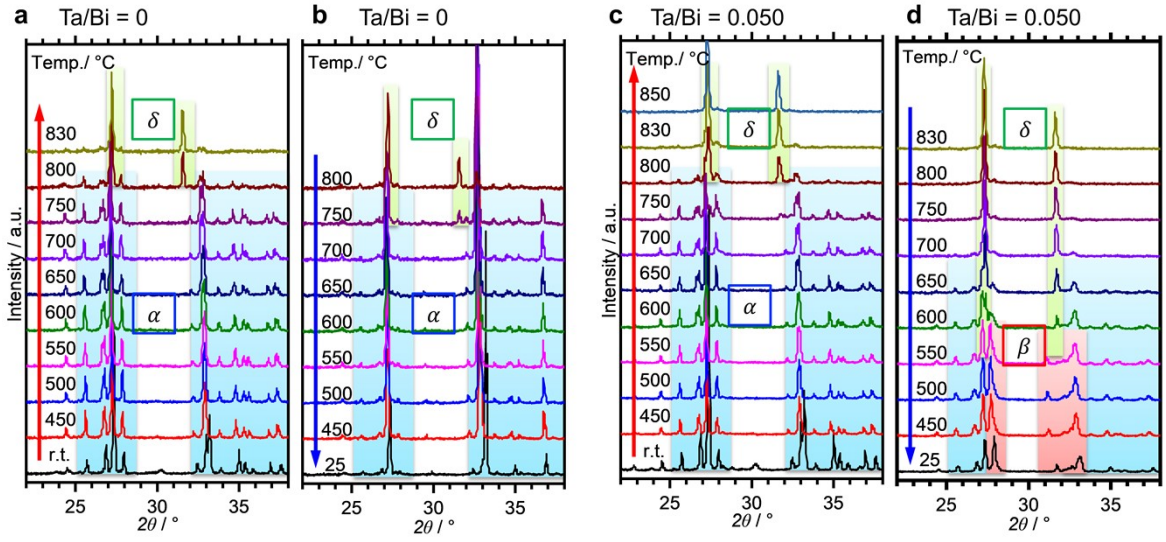

Figure 2. *In situ* high-temperature XRD for the Bi_2O_3 with Ta/Bi ratios of 0 (a and b) and 0.050 (c and d). The temperature was increased (a and c) and decreased (b and d) at the rate of 10 °C min^{-1} in static air. The assignments of the XRD peaks are indicated by coloring their backgrounds (blue: α phase; red: β phase; green: δ or cubic phase).

Figure 3a shows the XRD patterns of the samples with a much wider range of Ta/Bi ratios after cooling from the heat treatment at 850 °C for 5 h. Figure 3b shows the schematics of corresponding various crystal structures. The XRD patterns of α-, β-, δ-Bi_2O_3 and Bi_3TaO_7 from the inorganic crystal structure database (ICSD) are shown in Figure S1 as references. While no Ta_2O_5 addition led to the formation of the monoclinic α-Bi_2O_3 structure, a small addition of Ta (Ta/Bi ratio from 0.020 to 0.050) formed the β-Bi_2O_3 (tetragonal) structure. Further addition of Ta, to give rise to Ta/Bi ratio of 0.100, led to the formation of the δ phase of Bi_2O_3 (cubic, Pn-3 m). The samples with Ta/Bi = 0.167 and 0.333 were identified as the Bi_3TaO_7 phase (cubic, F-3 m). The principal XRD peaks of the obtained β-Bi_2O_3, δ-Bi_2O_3, and Bi_3TaO_7 phases are highlighted in Figure S2. It is of great significance to note that the amount of Ta from 2–5% did not influence the peak position of β-Bi_2O_3, suggesting the Bi and Ta atoms are not replacing each other in the crystal structures of our Ta-supplemented β-Bi_2O_3 samples in a way affects the lattice constant. On the other hand, for $Bi_{3-x}Ta_xO_{3+y}$ (x = 1.29) and Bi_3TaO_7 with the Ta/Bi ratio of 0.167 and 0.333 (Figure S2b), the main XRD peaks for (111) plane can be explained by the replacement of a Ta^{5+} cation with a Bi^{3+} cation, which is accompanied by the creation of oxygen vacancy for the charge compensation, and the overall charge electroneutrality of the system is preserved through a mechanism: $Bi^{3+} \rightarrow Ta^{5+} + O^{2-}$.[6] Finally, the studied samples are compiled in Table 1.

Table 1. Ta/Bi ratios in the prepared material, identification of the crystal phase, and the notation in this study.

Ta/Bi ratio	Crystal phase	Notation
0	α-Bi_2O_3 (monoclinic)	α-Bi_2O_3 (precursor)
0.020	β-Bi_2O_3 (tetragonal)	β-Bi_2O_3:Ta (2%)
0.026	β-Bi_2O_3 (tetragonal)	β-Bi_2O_3:Ta (2.6%)
0.033	β-Bi_2O_3 (tetragonal)	β-Bi_2O_3:Ta (3.3%)
0.050	β-Bi_2O_3 (tetragonal)	β-Bi_2O_3:Ta (5%)
0.100	δ-Bi_2O_3 (cubic, Pn-3 m)	δ-Bi_2O_3:Ta (10%)
0.167	Bi_3TaO_7 (cubic, Fm-3 m)	$Bi_{3+x}Ta_{1-x}O_{7-y}$ (x = 0.43)
0.333	Bi_3TaO_7 (cubic, Fm-3 m)	Bi_3TaO_7
–	Ta_2O_5 (orthorhombic)	Ta_2O_5 (precursor)

Figure S3 shows the SEM images and EDS mappings of the representative samples. Aggregated coarse particles with sizes on the order of micrometers somewhat thermally fused were observed in all samples. From EDX mapping, Bi, Ta, and O are well distributed throughout the particles for all samples, indicating the formation of a homogeneous solid solution or Ta-doped Bi_2O_3.

A small amount of added Ta was observed to play a significant role in structural determinations. To identify at which positions the Ta atoms are located in the crystal structures, the local environments of Bi and Ta atoms were studied with XAS measurements, including XANES and EXAFS. All spectra and their analyses are summarized in Figure S4. The Bi L_3-edge XANES spectra of α-Bi_2O_3 (reference), β-Bi_2O_3:Ta (5%), δ-Bi_2O_3:Ta (10%), and Bi_3TaO_7 are shown in Figure 4a. The spectral shape of the samples basically consists of a main absorption peak (A) located at 13.445 eV, a slight shoulder-like structure just below the main peak (A1, hv ~ 13.42 keV), and a single oscillation after the main peak (B, hv ~ 13.46 keV). The spectra of β-Bi_2O_3:Ta (5.0%), δ-Bi_2O_3:Ta (10.0%), and Bi_3TaO_7 show a hump (B, hv ~ 13.46 keV) followed by a negative feature at higher energies (C, hv ~ 13.47 keV), and the spectrum of α-Bi_2O_3 presents a wide plateau at the energy region immediately after the main peak (B–C, hv ~ 13.46–13.47 keV). This directly indicates that the local environments of Bi in the samples under study are different from those of α-Bi_2O_3. Moreover, the shift in the shoulder-like structure (A1, hv ~ 13.42 keV) at the edge (A, hv ~ 13.445 keV) and just below the edge (B, hv ~ 13.46 keV) cannot be explained with the linear combination of each other. In other words, the XANES profiles of the samples cannot be explained with the presence of mixed polymorphs.

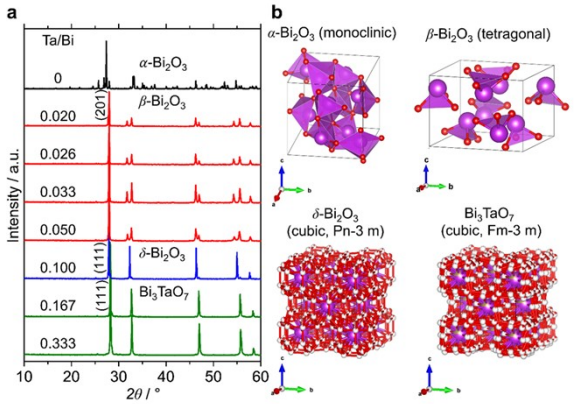

Figure 3. (a) XRD patterns of the samples at the Ta/Bi ratio. B) Schematics of the crystal structures from ICSD 94229 (α-Bi_2O_3), 417638 (β-Bi_2O_3), 38436 (δ-Bi_2O_3), and 161407 (Bi_3TaO_7).

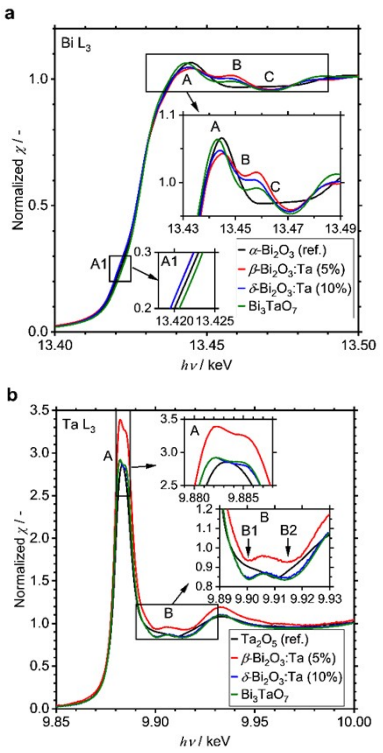

Figure 4. (a) Comparison of the experimental Bi L_3-edge of α-Bi_2O_3 (reference), β-Bi_2O_3:Ta (5%), δ-Bi_2O_3:Ta (10%), and Bi_3TaO_7. (b) Ta L_3-edge XANES spectra of Ta_2O_5 (reference), β-Bi_2O_3:Ta (5%), δ-Bi_2O_3:Ta (10%), and Bi_3TaO_7.

Next, the Ta L_3-edge XANES spectra of α-Bi_2O_3 (reference), β-Bi_2O_3:Ta (5%), δ-Bi_2O_3:Ta (10%), and Bi_3TaO_7 are shown in Figure 4b. All of the compounds show a main peak (A) at ~9.884 keV, but our samples have a double peak corresponding to the split of 5*d* orbitals, whereas the Ta_2O_5 reference show only a single peak. This difference is more apparent at the energy region immediately after the main peak because our samples show a hump (B, *hv* ~ 9.906 keV), whereas the Ta_2O_5 reference only shows a shoulder-like structure (B1, *hv* ~ 9.903 keV) followed by a negative feature at a higher energy (B2, *hv* ~ 9.910 keV). These comparison to the Ta_2O_5 reference shows that the local environments around Ta in our studied samples are different from those in the Ta_2O_5 reference. Similar results are reported in the W L_3-edge XANES spectra of Bi_2WO_6 (octahedral) and $Bi_{14}WO_{24}$ (tetrahedral) by Wind and coworkers[29] and the W L_3-edge XANES spectra of other W-related oxides by Yamazoe and coworkers.[44] It is reasonable to consider that the differences of the local environments around Ta in the Ta_2O_5 (reference) and our Bi–Ta oxides result from a distortion or oxygen vacancies in the crystal structure induced by Ta addition.

The characters of the structural orders around Bi and Ta in the samples are also inferred from the comparison of the Fourier transforms of the EXAFS signals. In Figure 5, Bi L_3 and Ta L_3 signals of Bi and Ta in the α-Bi_2O_3 reference, α-Bi_2O_3 precursor, and β-Bi_2O_3:Ta (5%) are compared. The main peak at ~1.7 Å and double peaks at ~3 Å shown in Figure 5b correspond to the first coordination shell made of oxygen atoms and Bi neighbors.[45] Additionally, those peaks could be explained by the theoretical radial distribution function calculated from the optimized crystal structures. Figure 5c shows the Ta L_3-edge EXAFS spectra of the Ta_2O_5 reference, Ta_2O_5 precursor, and β-Bi_2O_3:Ta (5%). The difference between the environments of Ta atoms in the Ta_2O_5 and our β-Bi_2O_3:Ta (5%) is suggested by the Fourier transforms shown in Figure 5d. The enhancement of the main peak (~ 1.5 Å) can be related to the distortions in distances and angles between the Ta–O bonds in the TaO_6 octahedra.[46] Furthermore, that distortion is also suggested by the shift of the main peak (~ 1.5 Å) and appearance of the second peak at ~ 2 Å.

The structural orders in the δ-Bi_2O_3:Ta (10%) and Bi_3TaO_7 and their crystal systems were also studied by both of Bi L_3 and Ta L_3 edge EXAFS spectra. The EXAFS spectra are shown in Figures 5a and 5c and their Fourier transforms are shown in Figures 5b and 5d. To calculate the theoretical simulation, we assumed that when a Ta atom substitutes Bi sites in the cubic lattice in such a way, that the Bi–O distance decreases, moving the O atoms close to the Bi. This substitutability of Bi and Ta leads to tunability of the bandgap of these cubic-phase B–Ta oxides, as is discussed later. One might initially contend that Ta^{5+} and Bi^{3+} cannot substitute each other in the crystal lattice because the charge in the oxide cannot be balanced. However, the charge has been reasonably explained to be balanced by the change in the occupancy of O sites in the previous studies.[5] Therefore, it can be concluded that by mixing Bi_2O_3 and Ta_2O_5 at the molar ratio of Ta/Bi = 0.1, 0.33, the resulting Bi–Ta oxides stabilized and formed a substitutional solid solution with the cubic crystal phase.

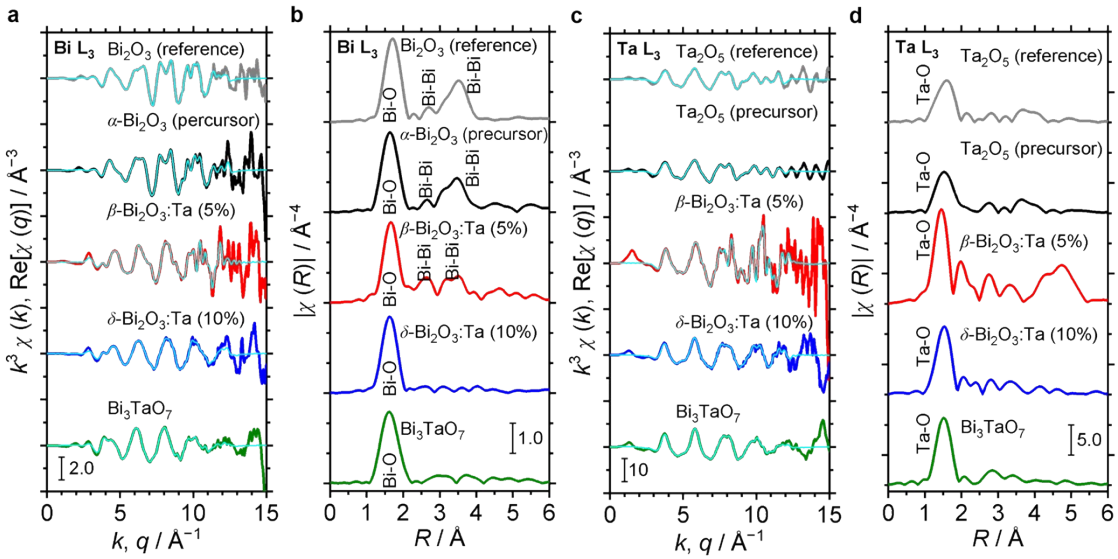

Figure 5. (a) Comparison of Bi L_3 EXAFS spectra of α-Bi_2O_3 (reference), α-Bi_2O_3 (precursor), β-Bi_2O_3:Ta (5%), δ-Bi_2O_3:Ta (10%) and Bi_3TaO_7. (b) Corresponding Fourier transforms. (c) Comparison of Ta L_3 EXAFS spectra of Ta_2O_5 (reference), Ta_2O_5 (precursor), β-Bi_2O_3:Ta (5%), δ-Bi_2O_3:Ta (10%) and Bi_3TaO_7. (d) Their corresponding Fourier transforms.

Electronic Structures and Optical Properties

The densities of states (DOS) and the charge density maps of β-Bi_2O_3 (201) and δ-Bi_2O_3 (111) slabs were computed using HSE06 (Heyd–Scuseria–Ernzerhof) exchange-correlation functional, and they are shown in Figure 6a. The VBM is dominated by O 2*p* states, whereas the CBM is mostly composed of O 3*s* and Bi 6*p* for β-Bi_2O_3 and Bi 6*p* for δ-Bi_2O_3. It is worth mentioning that the narrower bandgaps of β-Bi_2O_3 and δ-Bi_2O_3 were explained only by Bi and O, without contribution from the partial density of states of Ta. To study the qualitative nature of chemical bonding in (201) slab of β-Bi_2O_3 and (111) slab of δ-Bi_2O_3, the electron density distribution is presented in Figure 6b. Comparing these two model surfaces, we observe more depletion of charge on Bi in (111) δ-Bi_2O_3 and more σ character of bonds on the surface of δ-Bi_2O_3, while β-Bi_2O_3 exhibits mixed bonds. However, there is a lack of strong hybridization (observed also in DOS in Figure 6a) between Bi and O states in both surfaces; thus, fewer covalent bonds between atoms will exist, which could suppress the charge carrier transport. Moreover, we computed the effective mass tensors of the photogenerated holes (m_h^*) and electrons (m_e^*) at the band edges of (201) slab of β-Bi_2O_3 and (111) slab of δ-Bi_2O_3 using their electronic band structure, which were obtained from the PBE exchange-correlation functional; these results are listed in Table 2. The values are substantially larger than the benchmarking 0.5 m_0 for good charge carrier transport,[47–49] even compared to those based on the Bi–Ti–O system reported in our previous studies.[50, 51] Large values of both electron mass and hole effective mass for both (201) slab of β-Bi_2O_3 and (111) slab of δ-Bi_2O_3 predict poor charge separation capability of the materials and the resultant poor photocatalytic properties. The optimized structures and the local potential in the z-direction are shown in Figure S5.

Table 2. Summary of electronic, dielectric, and optical properties of (201) oriented β-Bi_2O_3 and (111) oriented δ-Bi_2O_3 slabs.

Bandgap (eV)	2.02	2.68
Electronic dielectric constant ε_∞ along: *xx (yy)*	6.0 (4.8)	5.0 (7.3)
Macroscopic dielectric constant ε_r along: *xx (yy)*	98 (93)	100 (119)
Effective electron mass m_e^*/m_e	1.2	3.2
Effective hole mass m_h^*/m_e	20	13
VBM (vs vacuum in eV)	–5.59	–5.36
CBM (vs vacuum in eV)	–3.46	–2.68
Bandgap (eV)	2.13	2.68
Electronic dielectric constant ε_∞ along: *xx (yy)*	6.0 (4.8)	5.0 (7.3)

To determine absorption characteristics of the Bi-based samples, DR-UV-vis spectroscopy was used and compared with the simulated absorption coefficient as a function of wavelength. The results are shown in Figure 7. The Kubelka-Munk functions of the representative ones (Figure 7a) show that for the pure α-Bi_2O_3 precursor, the adsorption edge was 445 nm in the near UV region, whereas that of β-Bi_2O_3:Ta (5%) was 550 nm. The absorption edges of the δ-Bi_2O_3:Ta (10%) and Bi_3TaO_7 were 530 and 440 nm, respectively. The bandgap energy calculation yields values of 2.8, 2.2, 2.3, and 2.8 eV for α-Bi_2O_3, β-Bi_2O_3:Ta (5%), δ-Bi_2O_3:Ta (10%), and Bi_3TaO_7, respectively. The visible-light responsiveness of β-Bi_2O_3 and δ-Bi_2O_3 were simulated on our slab models whose structures were optimized without adding Ta. The simulated absorption spectra are shown in Figure 7b, and their absorption edges nearly corresponded to those of the experimental spectra. In general, the degree of absorption coefficient is considered low for these

Bi_2O_3, compared to other general compound-based semiconductors.[47]

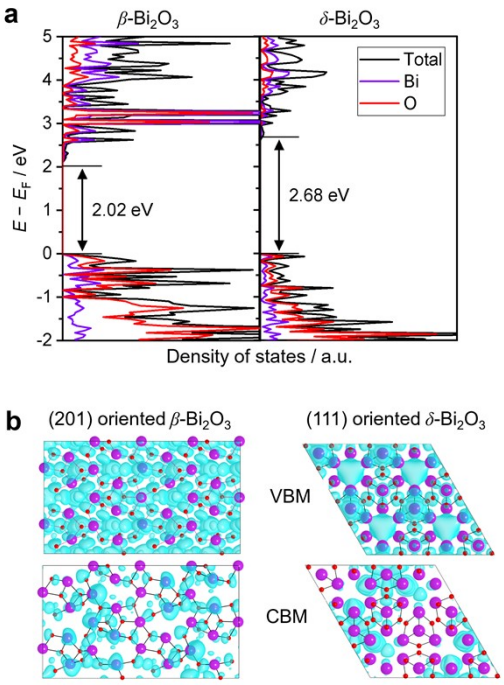

Figure 6. (a) The total and partial electronic density of states (DOS) of a (201) slab of β-Bi_2O_3 and a (111) slab of δ-Bi_2O_3. The geometry optimization and electronic structure calculations were performed employing the HSE06 (Heyd–Scuseria–Ernzerhof) exchange-correlation functional along with spin-orbit coupling (SOC) corrections, as implemented in VASP (Vienna Ab initio Simulation Package). (b) Charge density maps obtained for VBM and CBM electronic states of the (201) β-Bi_2O_3 and (111) δ-Bi_2O_3 slabs. The isosurface value is set at 6.7×10^{-3} au.

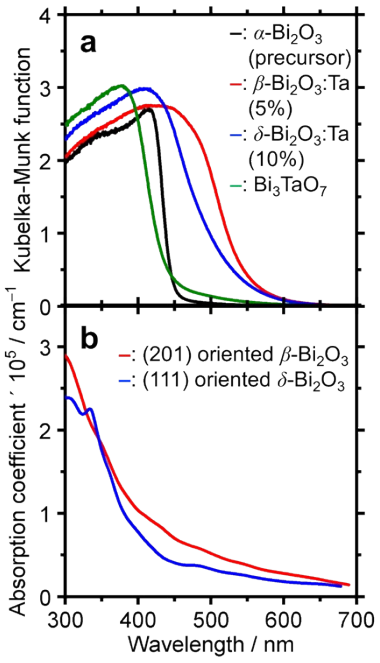

Figure 7. (a) The DR-UV-vis spectroscopy of α-Bi_2O_3 (precursor), β-Bi_2O_3:Ta (5%), δ-Bi_2O_3:Ta (10%), and Bi_3TaO_7. (b) Simulated UV-visible optical absorption spectra for (201) oriented β-Bi_2O_3 and (111) oriented δ-Bi_2O_3 slabs.

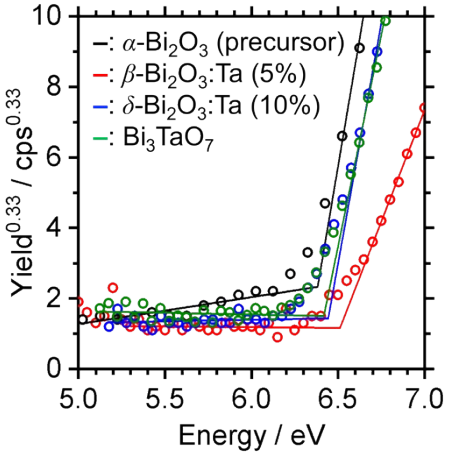

Figure 8. Photoelectron spectroscopy in air (PESA) of α-Bi_2O_3 (precursor), β-Bi_2O_3:Ta (5%), δ-Bi_2O_3:Ta (10%), and Bi_3TaO_7.

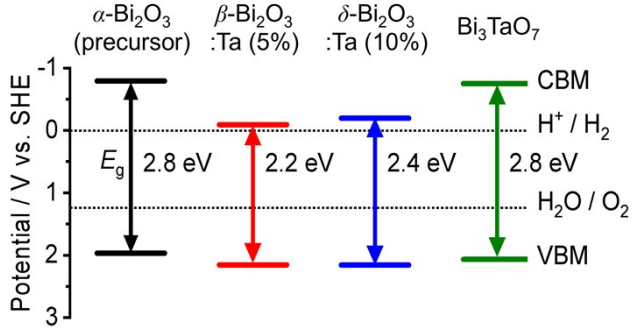

Figure 9. The experimental band positions of α-Bi_2O_3 (precursor), β-Bi_2O_3:Ta (5%), δ-Bi_2O_3:Ta (10%), and Bi_3TaO_7. The bandgap (E_g) and valence band maximum (VBM) of each sample were determined by DR-UV-vis spectroscopy (Figure 7a) and photoelectron spectroscopy in air (PESA) (Figure 8), respectively.

Because it remained possible that the visible-light responsiveness (2.2 eV bandgap) is derived from the existence of defects especially caused by added Ta in the β-Bi_2O_3:Ta (5%), photoluminescence spectroscopy was conducted. The results are shown in Figure S6. For the α-Bi_2O_3 (precursor) shown in Figure S6a, the emission spectra triggered by 400 nm excitation light showed a peak at 500–700 nm attributable to the existence of a defect level within the bandgap. However, the photoluminescence spectrum of our β-Bi_2O_3:Ta (5%) shown in Figure S6b did not exhibit noticeable peaks other than a small peak at 560 nm attributed to near bandgap emission. This result does not contradict the statement that the photon absorption at band edges is mainly β-Bi_2O_3 bandgap excitation.

The band alignment of the CBM and the VBM positions of the synthesized samples were experimentally estimated by using PESA. The VBM potentials estimated by ionization potentials were obtained by the crossing point of the linear part of the curve with the background from PESA. The spectra of

representative samples are shown in Figure 8, and all other spectra of the Bi–Ta oxides are shown in Figure S7. The VBMs do not shift significantly but remain constant at 6.4–6.6 eV vs. vacuum (i.e., 2.0–2.2 eV vs. SHE), as expected from the contribution of O 2*p* orbitals. The determined band positions are summarized in Figure 9 together with the Ta/Bi ratio and the resulting crystal phase. The results suggest that the conduction band positions are largely altered while valence band positions are relatively consistent.

To check the photoresponsive behavior of α-Bi_2O_3 (precursor) and β-Bi_2O_3:Ta (5%), the LSV (linear sweep voltammetry) under chopped-light illumination was recorded for CoO_x/α-Bi_2O_3 (precursor)/Ti–Sn, and CoO_x/β-Bi_2O_3:Ta (5%)/Ti–Sn particle–transferred electrodes. The result is shown in Figure 10. The CoO_x/α-Bi_2O_3 (precursor)/Ti–Sn electrode did not exhibit a pronounced response to the light, but the CoO_x/β-Bi_2O_3:Ta (5%)/Ti–Sn electrode showed a pronounced anodic photocurrent. Because the Xe-lamp was used with a cut-off filter as the light source (420 < λ < 650 nm), this spectrum indicates that this material can utilize visible light to produce photo-excited holes and electrons. The onset potential of the sacrificial reagent oxidation reaction was found to be 0.5 V vs. RHE under the light illumination, despite the fact that it was 1.0 V vs. RHE in dark conditions. The anodic photocurrent of 0.1 mA cm^{-2} was exhibited at 1.25 V vs. RHE.

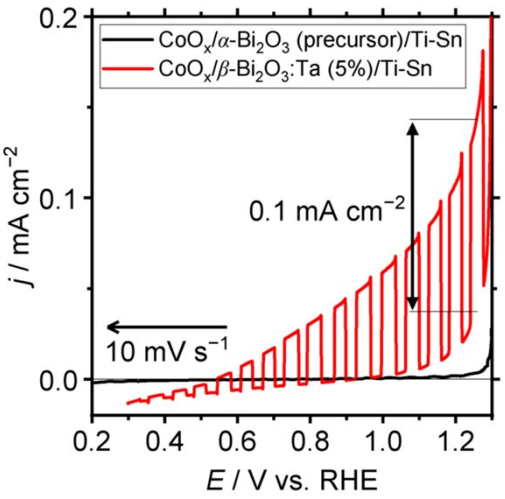

Figure 10. LSV at 10 mV s^{-1} under light chops for CoO_x/α-Bi_2O_3 (precursor)/Ti–Sn and CoO_x/β-Bi_2O_3:Ta (5%)/Ti–Sn in 1 M potassium borate aqueous solution (pH 9). Sacrificial reagent: 0.1 M Na_2SO_3; RE: Hg/Hg_2Cl_2/saturated KCl; CE: Pt wire; light source: Xe-lamp (MAX-303, 300 W) with cut-off filter (L42), > 420 nm; temperature: 25 °C.

Table 3. Summary of the computed properties for β-Bi_2O_3 and δ-Bi_2O_3.

		(201) β-Bi_2O_3	(111) δ-Bi_2O_3
ε_∞	along *x*	6.0	5.0
	along *y*	4.8	7.3
ε_{vib}	along *x*	98	100
	along *y*	93	119
m_e^* / m_e		1.2	3.2
m_h^* / m_e		19.9	12.5

To determine the dielectric properties of β-Bi_2O_3:Ta (5%) and δ-Bi_2O_3:Ta (10%), we computed their dielectric constants and effective masses. In a dielectric material, the static dielectric constant (ε_r) has contributions from two factors: the electron density (ε_∞) and the ion vibrations (ε_{vib}). The dielectric constants and effective masses are listed in Table 3, and the real and imaginary parts of the dielectric functions obtained HSE06 and SOC are shown in Figure S8. With these calculations, the charge carriers were found to be heavy, indicating poor photocatalytic properties.

Thermal Redox Properties

To investigate the difference of reducibility of our Bi-based oxides and consider an application for them as a material that is accompanied by thermal redox, TPR measurements were performed. The TPR profiles of the studied Bi–Ta oxides are shown in Figure 11. A broad reduction peak of α-Bi_2O_3 (precursor) appeared at 700 °C. The atomic ratio of consumed H_2 to Bi contained in the sample (H_2/Bi ratio, Figure 11) was calculated to be 1.58, and the total hydrogen consumption accounted for the complete reduction of the α-Bi_2O_3 (precursor) sample. The broadness of the peak can be attributed to the relatively large sizes of the α-Bi_2O_3 (precursor) particles, as seen in the SEM images (Figure S3). The peak was tailed to 400 °C, suggesting a faster reduction of the surface. TPR was also performed on the Ta_2O_5 (precursor), but substantial reduction was not observed throughout this temperature range up to 900 °C. β-Bi_2O_3:Ta (5%) showed reduction starting at around 400 °C, with a maximum at 640 °C, indicating facilitated reduction compared to α-Bi_2O_3 (precursor). Both the H_2/Bi and H_2/O ratios of 1.56 and 0.96 indicated the complete reduction of Bi atoms. δ-Bi_2O_3:Ta (10%) had a reduction peak starting at 300 °C, a markedly low temperature, with a maximum at 520 °C, again the lowest temperature among the samples investigated. These findings suggest that reduction of both bulk and the surface of δ-Bi_2O_3:Ta (10%) was easiest among the samples. This facilitated redox property might be explained by the high mobility of oxygen species related to the low occupancy of O sites due to its defective crystal structure. The consumption of hydrogen (H_2/Bi = 1.53 and H_2/O = 0.88) can be explained if it is assumed that the Ta atoms are not reduced, and that only Bi atoms are reduced, as expressed by the following reaction (note that δ-Bi_2O_3:Ta [10%] is expressed as $Bi_2Ta_{0.2}O_{3.5}$):

$$Bi_2Ta_{0.2}O_{3.5} + 3H_2 \rightarrow 2Bi + 3H_2O + 0.1Ta_2O_5 \quad (1)$$
(H_2/Bi = 3/2 = 1.5, H_2/O = 3/3.5 = 0.857)

Bi_3TaO_7 showed a reduction peak at 640 °C, which appeared at a higher temperature than that of δ-Bi_2O_3:Ta (10%); this may be because δ-Bi_2O_3:Ta (10%) has a less defective structure than that of Bi_3TaO_7. The peak was tailed to 300 °C, but the tailing was not as pronounced as that of δ-Bi_2O_3:Ta (10%). The stoichiometry of the consumption of hydrogen (H_2/Bi = 1.68 and H_2/O = 0.72) can be roughly explained by the following reaction:

$$Bi_3TaO_7 + 4.5H_2 \rightarrow 3Bi + 4.5H_2O + 0.5Ta_2O_5 \quad (2)$$
(H_2/Bi = 4.5/3 = 1.5, H_2/O = 4.5/7 = 0.643)

Among these oxides, δ-Bi_2O_3:Ta (10%) appeared to have a TPR peak at the lowest temperature, meaning the highest thermal redox property. This material is expected to be utilized as a catalyst or its support for reactions that are accompanied by oxidation or reduction. Further investigations into the applications of this material as a thermal catalyst or its support are expected.

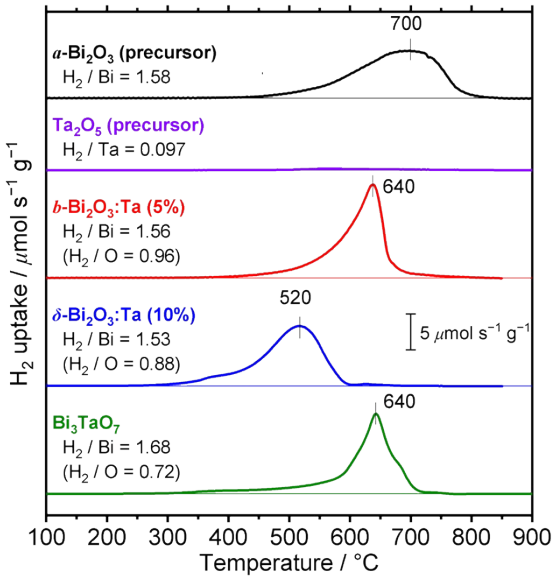

Figure 11. TPR profiles of α-Bi_2O_3 (precursor), Ta_2O_5 (precursor), β-Bi_2O_3:Ta (5%), δ-Bi_2O_3:Ta (10%), and Bi_3TaO_7. The total hydrogen consumptions are expressed in moles of H_2 consumed per mole of metal atoms (H_2/Bi or H_2/Ta) and moles of H_2 consumed per mole of O atoms (H_2/O). The samples were pretreated in Ar (20 mL min^{-1}) at 400 °C before each measurement. The measurements were conducted on 20 mg of samples in 4% H_2 (in Ar, 20 mL min^{-1}) with a heating rate of 10 °C min^{-1}.

Conclusions

In summary, this investigation of the Ta-supplemented bismuth oxides, such as α-Bi_2O_3, β-Bi_2O_3, δ-Bi_2O_3 and Bi_3TaO_7, confirms that the crystal structures and optoelectronic properties of these oxides are altered according to the amount of added Ta (as Ta_2O_5). Heat treatment at 850 °C and cooling of Bi_2O_3 with different amounts of added Ta controllably led to the formation of α-Bi_2O_3, β-Bi_2O_3, and δ-Bi_2O_3. Among them, β-Bi_2O_3 was found to be a promising visible-light harvesting material, as it has the narrowest bandgap of 2.2 eV. DFT calculations using the HSE exchange-correlation functional and PESA measurements demonstrate that the conduction band has a large contribution from Bi orbitals in the β-Bi_2O_3 and the δ-Bi_2O_3. We confirmed that the presence of added Ta is not essential to alter the band structures of the bismuth oxides by causing a defect level but, rather, by changing the crystal phase of the bismuth oxides. However, the DFT calculations also suggested that β-Bi_2O_3 and δ-Bi_2O_3, which have bandgaps narrow enough to absorb a visible light, are limited in their applicability as a photocatalyst due to their large effective masses and resultant low charge mobilities. In addition, different Bi_2O_3 polymorphs exhibited distinctive reducibility upon hydrogen treatment at high temperatures, showing that δ-Bi_2O_3 was reduced at the lowest temperature among the samples investigated. The wide range of methodologies adopted in this study and the knowledge gained into the semiconductor structure of a mixed oxide through these methodologies will allow us to identify and understand other novel candidate materials for applications such as photocatalysis and thermal catalysis.

Author Contributions

All authors contributed to writing the manuscript. All authors approved the final version of the manuscript.

Conflicts of interest

There are no conflicts to declare.

Acknowledgements

This work was supported by the Mohammed bin Salman Center for Future Science and Technology for Saudi-Japan Vision 2030 at the University of Tokyo (MbSC2030). LC and RA acknowledge Shaheen and HPC Core Labs team at KAUST.

Notes and references

1 J. S. Ahn, M. A. Camaratta, D. Pergolesi, K. T. Lee, H. Yoon, B. W. Lee, D. W. Jung, E. Traversa and E. D. Wachsman, *J. Electrochem. Soc.*, 2010, **157**, B376.
2 R. D. Bayliss, S. N. Cook, S. Kotsantonis, R. J. Chater and J. A. Kilner, *Adv. Energy Mater.*, 2014, **4**, 1301575.
3 X. Kuang, J. L. Payne, M. R. Johnson and I. Radosavljevic Evans, *Angew. Chem. Int. Ed.*, 2012, **51**, 690–694.
4 R. Punn, A. M. Feteira, D. C. Sinclair and C. Greaves, *J. Am. Chem. Soc.*, 2006, **128**, 15386–15387.
5 K. Firman, K. B. Tan, C. C. Khaw, Z. Zainal, Y. P. Tan and S. K. Chen, *J. Mater. Sci.*, 2017, **52**, 10106–10118.
6 M. Gambino, F. Giannici, A. Longo, S. Di Tommaso, F. Labat and A. Martorana, *J. Phys. Chem. C*, 2015, **119**, 26367–26373.
7 R. Oka, Y. Shobu and T. Masui, *ACS Omega*, 2019, **4**, 7581–7585.
8 M. Li, F. Li and P. G. Yin, *Chem. Phys. Lett.*, 2014, **601**, 92–97.
9 S. J. A. Moniz, D. Bhachu, C. S. Blackman, A. J. Cross, S. Elouali, D. Pugh, R. Q. Cabrera and S. Vallejos, *Inorg. Chim. Acta*, 2012, **380**, 328–335.
10 M. Schlesinger, S. Schulze, M. Hietschold and M. Mehring, *Dalton Trans.*, 2013, **42**, 1047–1056.
11 Y. Lu, Y. Zhao, J. Zhao, Y. Song, Z. Huang, F. Gao, N. Li and Y. Li, *Cryst. Growth Des.*, 2015, **15**, 1031–1042.
12 L. Zhang, Y. Shi, Z. Wang, C. Hu, B. Shi and X. Cao, *Appl. Catal. B*, **2020**, *265*, 118563.
13 S. Singh and R. Sharma, *Sol. Energy Mater. Sol. Cells* **2018**, *186*, 208–216.
14 Y. C. Wu, Y. C. Chaing, C. Y. Huang, S. F. Wang and H. Y. Yang, *Dyes Pigm.*, 2013, **98**, 25–30.
15 S. Zhong, S. Zou, X. Peng, J. Ma and F. Zhang, *J. Sol-Gel Sci. Technol.*, 2015, **74**, 220–226.
16 H. Sudrajat, *J. Nanopart. Res.*, 2017, **19**, 1–8.
17 J. C. Medina, M. Bizarro, P. Silva-Bermudez, M. Giorcelli, A. Tagliaferro and S. E. Rodil, *Thin Solid Films*, 2016, **612**, 72–81.

18 H. Sudrajat and P. Sujaridworakun, *Mater. Des.*, 2017, **130**, 501–511.
19 S. Zhu, L. Lu, Z. Zhao, T. Wang, X. Liu, H. Zhang, F. Dong and Y. Zhang, *J. Phys. Chem. C*, 2017, **121**, 9394–9401.
20 H. Sudrajat and S. Hartuti, *Adv. Powder Technol.*, 2019, **30**, 983–991.
21 S. J. A. Moniz, C. S. Blackman, C. J. Carmalt and G. Hyett, *J. Mater. Chem.*, 2010, **20**, 7881–7886.
22 G. D. Lim, J. H. Yoo, M. Ji and Y. I Lee, *J. Alloys Compd.*, 2019, **806**, 1060–1067.
23 C. Chang, H.-C. Yang; N. Gao and S.-Y Lu, *J. Alloys Compd.*, 2018, **738**, 138–144.
24 N. R. Khalid, Z. Israr, M. B. Tahir and T. Iqbal, *Int. J. Hydrog. Energy*, 2020, **45**, 8479–8489.
25 Y. Shi, L. Luo, Y. Zhang, Y. Chen, S. Wang, L. Li, Y. Long and F. Jiang, *Ceram. Int.*, 2017, **43**, 7627–7635.
26 H. Sudrajat, *Superlattices Microstruct.*, 2017, **109**, 229–239.
27 A. H. Zahid and Q. Han, *Nanoscale*, 2021, **13**, 17687–17724.
28 G. Guenther and O. Guillon, *J. Mater. Res.*, 2014, **29**, 1383–1392.
29 J. Wind, J. Polt, Z. Zhang, D. A. Blom, T. Vogt, R. L. Withers and C. D. Ling, *Chem. Mater.*, 2017, **29**, 9171–9181.
30 V. Fruth, A. Ianculescu, D. Berger, S. Preda, G. Voicu, E. Tenea and M. Popa, *J. Eur. Ceram. Soc.*, 2006, **26**, 3011–3016.
31 H. N. Lin, M. S. Chen, Y. H. Chang, P. Y. Lee and C. K Lin, *Materials*, 2019, **12**, 12, 1947.
32 J. L. Ortiz-Quinonez, I. Zumeta-Dubé, D. Díaz, N. Nava-Etzana, E. Cruz-Zaragoza and P. Santiago-Jacinto, *Inorg. Chem.*, 2017, **56**, 3394–3403.
33 J. A. H. Dreyer, S. Pokhrel, J. Birkenstock, M. G. Hevia, M, Schowalter, A. Rosenauer, A. Urakawa, W. Y. Teoh and L. Mädler, *CrystEngComm*, 2016, **18**, 2046–2056.
34 W. Humphrey, A. Dalke and K. Schulten, *J. Mol. Graph.*, 1996, **14**, 33–38.
35 W. M. H. Sachtler, G. J. H. Dorgelo and A. A. Holscher, *Surf. Sci.*, 1966, **5**, 221–229.
36 G. Kresse and J. Hafner, *Phys. Rev. B*, 1993, **48**, 13115–13118.
37 G. Kresse, J. Furthmüller, *Phys. Rev. B*, 1996, **54**, 11169–11186.
38 P. E. Blöchl, *Phys. Rev. B*, 1994, **50**, 17953–17979.
39 H. J. Monkhorst and J. D. Pack, *Phys. Rev. B*, 1976, **13**, 5188–5192.
40 J. P. Perdew and Y. Wang, *Phys. Rev. B*, 1992, **45**, 13244–13249.
41 J. Heyd and G. E. Scuseria, *J. Chem. Phys.*, 2004, **121**, 1187–1192.
42 J. E. Peralta, J. Heyd, G. E. Scuseria and R. L. Martin, *Phys. Rev. B*, 2006, **74**, 073101.
43 M. Gmitra, S. Konschuh, C. Ertler, C. Ambrosch-Draxl and J. Fabian, *Phys. Rev. B*, 2009, **80**, 235431.
44 S. Yamazoe, Y. Hitomi, T. Shishido and T. Tanaka, *J. Phys. Chem. C*, 2008, **112**, 6869–6879.
45 M. A. Laguna-Marco, C. Piquer, A. G. Roca, R. Boada, M. Andrés-Vergés, S. Veintemillas-Verdaguer, C. J. Serna, A. Iadecola and J. Chaboy, *Phys. Chem. Chem. Phys.*, 2014, **16**, 18301–18310.
46 J. Ribeiro, G. Tremiliosi-Filho, P. Olivi and A. R. Andrade, *Mater. Chem. Phys.* **2011**, *125*, 449–460.
47 O. Madelung, *Semiconductors: Data Handbook,* Springer, Berlin Heidelberg, 2012.
48 S. Adachi, *GaAs and Related Materials: Bulk Semiconducting and Super-lattice Properties*, World Scientific, 1994.
49 T. Le Bahers, M. Rérat and P. Sautet, *J. Phys. Chem. C*, 2014, **118**, 5997–6008.
50 S. Lardhi, D. Noureldine, M. Harb, A. Ziani, L. Cavallo and K. Takanabe, *J. Chem. Phys.*, 2016, **144**, 134702.
51 D. Noureldine, S. Lardhi, A. Ziani, M. Harb, L. Cavallo and K. Takanabe, *J. Mater. Chem. C*, 2015, **3**, 12032–12039.